



**HAL**  
open science

# Quantitative Visualization of Thermally Enhanced Perpendicular Shape Anisotropy STT-MRAM Nanopillars

Trevor P. Almeida, Alvaro Palomino, Steven Lequeux, Ricardo C. Sousa, Olivier Fruchart, Ioan Lucian Prejbeanu, Bernard Diény, Aurélien Masseboeuf, David Cooper

► **To cite this version:**

Trevor P. Almeida, Alvaro Palomino, Steven Lequeux, Ricardo C. Sousa, Olivier Fruchart, et al.. Quantitative Visualization of Thermally Enhanced Perpendicular Shape Anisotropy STT-MRAM Nanopillars. *Nano Letters*, 2022, 22 (10), pp.4000. 10.1021/acs.nanolett.2c00597 . hal-03553914v2

**HAL Id: hal-03553914**

**<https://hal.science/hal-03553914v2>**

Submitted on 23 May 2022

**HAL** is a multi-disciplinary open access archive for the deposit and dissemination of scientific research documents, whether they are published or not. The documents may come from teaching and research institutions in France or abroad, or from public or private research centers.

L'archive ouverte pluridisciplinaire **HAL**, est destinée au dépôt et à la diffusion de documents scientifiques de niveau recherche, publiés ou non, émanant des établissements d'enseignement et de recherche français ou étrangers, des laboratoires publics ou privés.



Distributed under a Creative Commons Attribution 4.0 International License

1 **Quantitative visualization of thermally-enhanced perpendicular shape**  
2 **anisotropy STT-MRAM nano-pillars**

3 Trevor P. Almeida<sup>1,2\*</sup>, Steven Lequeux<sup>3</sup>, Alvaro Palomino<sup>3</sup>, Ricardo C. Sousa<sup>3</sup>, Olivier  
4 Fruchart<sup>3</sup>, Ioan Lucian Prejbeanu<sup>3</sup>, Bernard Dieny<sup>3</sup>, Aurélien Masseboeuf<sup>3</sup> and David Cooper<sup>1</sup>

5  
6 <sup>1</sup>Univ. Grenoble Alpes, CEA, Leti, F-38000 Grenoble, France.

7 <sup>2</sup>SUPA, School of Physics and Astronomy, University of Glasgow, G12 8QQ, UK.

8 <sup>3</sup>Univ. Grenoble Alpes, CEA, CNRS, Grenoble INP, SPINTEC, 38000 Grenoble, France.

9

10

11

12

**Abstract**

13 Perpendicular shape anisotropy (PSA) offers a practical solution to downscale spin-transfer  
14 torque Magnetic Random-Access Memory (STT-MRAM) beyond the sub-20 nm technology  
15 node whilst retaining thermal stability. However, our understanding of the thermomagnetic  
16 behavior of PSA-STT-MRAM is often indirect, relying on magnetoresistance measurements  
17 and micromagnetic modelling. Here, the magnetism of a NiFe PSA-STT-MRAM nano-pillar is  
18 investigated using off-axis electron holography, providing spatially resolved magnetic  
19 information as a function of temperature. Magnetic induction maps reveal the micromagnetic  
20 configuration of the NiFe storage layer (~ 60 nm high,  $\leq 20$  nm diameter), confirming the PSA  
21 induced by its 3:1 aspect ratio. *In-situ* heating demonstrates that the PSA of the storage layer is  
22 maintained up to at least 250 °C, and direct quantitative measurements reveal a moderate  
23 decrease of magnetic induction. Hence, this study shows explicitly that PSA provides  
24 significant stability in STT-MRAM applications that require reliable performance over a range  
25 of operating temperatures.

26

27

28 Keywords: Perpendicular shape anisotropy STT MRAM; nanomagnetism; off-axis electron  
29 holography; thermomagnetic stability

30

31

\*Corresponding author:

32

Tel: +44 (0) 141 330 4712

33

Email: trevor.almeida@glasgow.ac.uk

## 1 **1. Introduction**

2 Magnetoresistive random-access memory (MRAM) is a type of non-volatile memory based on  
3 the storage of bits of information by magnetic cells with controllable polarity<sup>1</sup>. The discovery  
4 of the spin-transfer torque (STT) effect has made MRAM industrially relevant, thanks to the  
5 ability to write cells with an electric current<sup>2-5</sup>. STT-MRAM can be easily integrated with  
6 CMOS technology<sup>6</sup>, has low energy consumption<sup>7</sup>, superior endurance<sup>7,8</sup>, and rather high areal  
7 density<sup>9</sup>. In practice, STT-MRAM involves the use of a magnetic tunnel junction (MTJ)  
8 comprising two perpendicularly-magnetized ferromagnetic plates (one magnetically-pinned  
9 reference layer and one switchable storage layer) separated by a thin insulating MgO tunnel  
10 barrier (1 – 1.5 nm thick) . This design is called p-STT-MRAM, the perpendicular anisotropy  
11 resulting from interfacial electronic hybridization effects occurring at the interface between the  
12 magnetic electrodes and the oxide tunnel barrier<sup>10</sup>. MTJs provide a useful system of readable /  
13 writable ‘0’ or ‘1’ binary information, as its electrical resistance changes significantly when the  
14 layers are magnetized in parallel and antiparallel states,. Increasing the areal bit density of p-  
15 STT-MRAM requires to reduce the in-plane size or diameter of the nano-patterned MTJ<sup>11</sup>.  
16 However, below a characteristic magnetic length scale around 20nm, this comes with an  
17 excessive decrease of the thermal stability of the magnetic moment of the ultrathin storage  
18 layer. Perpendicular shape anisotropy (PSA) offers an innovative solution by increasing the  
19 storage layer thickness to larger than its diameter, so that its out-of-plane aspect ratio combined  
20 with large volume provides additional thermal stability<sup>12,13</sup>. PSA-STT-MRAM has been shown  
21 previously to indeed be highly thermally stable, making them a practical solution to downsize  
22 scalability of STT-MRAM at sub-20 nm technology nodes<sup>14,15</sup>. However, our knowledge of the  
23 thermal stability of these STT-MRAM nano-pillars is often indirect, relying on  
24 magnetoresistance measurements and micromagnetic modelling. In order to understand fully  
25 their thermomagnetic behavior, it is necessary to examine the effect of temperature directly.  
26 The advanced transmission electron microscopy (TEM) technique of off-axis electron  
27 holography allows imaging of magnetization within nano-scale materials, with high spatial  
28 resolution and sensitivity to induction field components transverse to the electron beam<sup>16</sup>.  
29 Combining electron holography with *in-situ* heating within the TEM has already allowed direct  
30 imaging of the thermal stability of nano-scale signal carriers and fields of magnetic minerals<sup>17-</sup>  
31 <sup>19</sup>, meteorites<sup>20</sup> and pre-patterned MTJ conducting pillars<sup>21</sup>.

32 In this paper, we use electron holography to image the micromagnetic configuration of an  
33 individual  $\leq 20$  nm diameter FeCoB / NiFe STT-MRAM nano-pillar and acquire quantitative

1 measurements of magnetic induction from the high-aspect-ratio FeCoB / NiFe composite free  
2 layer. In addition, we experimentally demonstrate the influence of PSA on its thermal stability  
3 through *in-situ* heating within the TEM to 250 °C. This study provides direct evidence of the  
4 PSA exhibited by the high-aspect-ratio free layer, and its improved thermal stability compared  
5 to standard p-STT-MRAM.

6

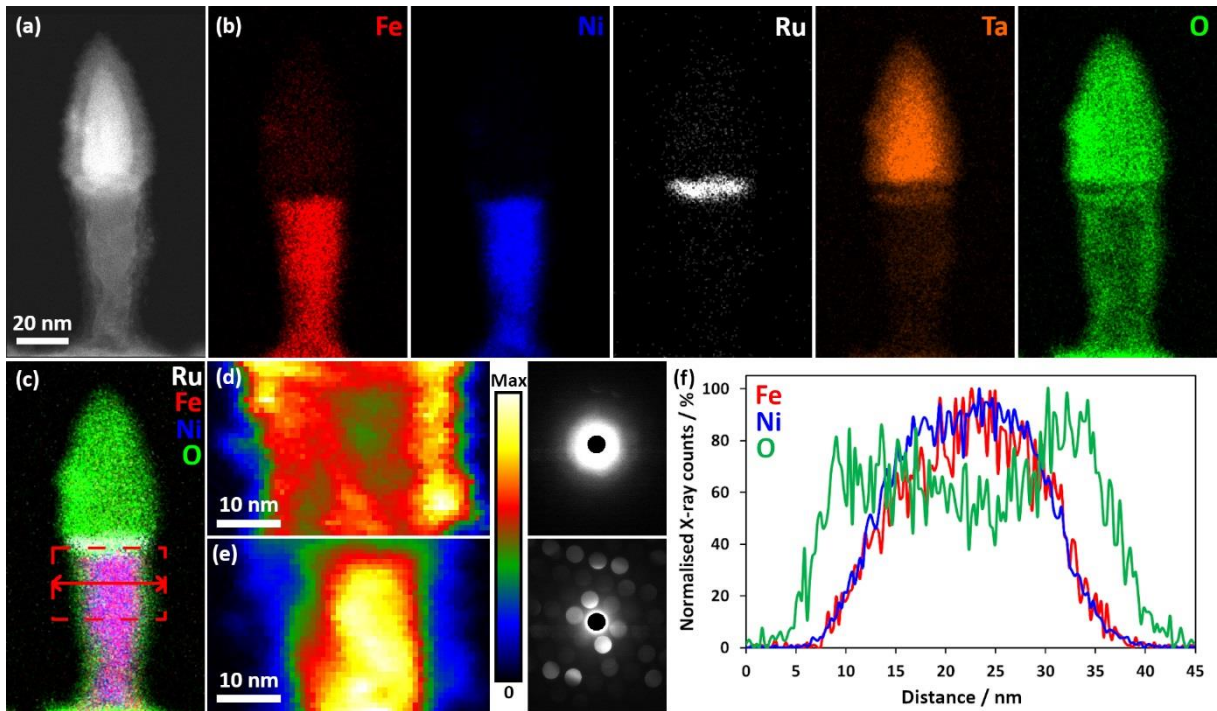
## 7 **2. Experimental**

8 An array of FeCoB / NiFe PSA-STT-MRAM nano-pillars was fabricated through sequential e-  
9 beam lithography, reactive ion etching and ion beam etching<sup>12</sup>. The full stack of PSA MTJs has  
10 the following composition: SiO<sub>2</sub> / Pt (25 nm) / SAF / Ta (0.3 nm) / FeCoB (1.1 nm) / MgO (1.2  
11 nm) / FeCoB (1.4 nm) / W (0.2 nm) / NiFe (60 nm) / Ta (1 nm) / Ru (3 nm) / Ta (150 nm), where  
12 the thick NiFe layer provides the PSA<sup>12,14</sup>. SAF stands for a synthetic antiferromagnet,  
13 providing a compensated-moment antiferromagnetically-pinned magnetic reference as the  
14 bottom layer. A protective layer of organic resin (~ 1 μm) was spin-coated onto the array prior  
15 to being inserted into a Thermo Fisher Strata 400S dual-beam focused ion beam (FIB) /  
16 secondary electron microscope (SEM) for TEM sample preparation. A protective W layer was  
17 deposited over the resin and trenches were FIB irradiated until a ~ 3 μm × ~ 20 μm lamella was  
18 prepared and transferred to Omniprobe copper lift-out grids, where it was thinned to a thickness  
19 of ~ 300 nm using conventional FIB methods. The protective resist layer was etched away using  
20 a plasma cleaner and the remaining W layer was broken off with the micromanipulator. High  
21 angle annular dark field (HAADF) scanning TEM (STEM) imaging was performed using a  
22 probe-C<sub>s</sub>-corrected Thermo Fisher Titan TEM with an accelerating voltage of 200kV.  
23 Corresponding chemical analysis was provided by energy dispersive X-ray (EDX)  
24 spectroscopy using a Super-X EDX system whose geometry consists of four Bruker silicon drift  
25 detectors. A Thermo Fisher Titan TEM equipped with an image-C<sub>s</sub> corrector and an electron  
26 biprism was used to perform off-axis electron holography. Electron holograms were acquired  
27 under field-free conditions in Lorentz mode on a Gatan OneView 4K camera. A voltage of 220  
28 V was applied to the biprism, resulting in an interference fringe spacing of ~ 1.7 nm. Stacks of  
29 8 electron holograms (each acquired for 4s) were aligned and then averaged using the Holoview  
30 software<sup>22</sup> to improve the signal to noise ratio of the reconstructed phase images. The  
31 magnetization states of the nano-pillars were visualized through separation of the magnetic  
32 contribution to the phase shift from the mean inner potential (MIP), achieved by tilting to ± 40°  
33 and applying the strong field of the objective lens (< 1.5 T) to reverse the magnetic

1 contribution<sup>23</sup>. *In-situ* heating up to 250°C was performed using a Gatan heating holder under  
2 field-free magnetic conditions, allowing 30 minutes to stabilize from thermal drift at each  
3 temperature interval. The heating was repeated and the magnetic reversal was performed at  
4 each temperature interval to isolate the MIP, and subtracted from the first heating to reconstruct  
5 the thermomagnetic behavior of the nano-pillars<sup>18,19</sup>. For the construction of magnetic induction  
6 maps, the cosine of the magnetic contribution to the phase shift was amplified ( $\times 150$ ) to  
7 produce magnetic phase contours and arrows were added to show the direction of the projected  
8 induction.

### 9 10 **3. Results**

11 Figure 1 presents the chemical composition, morphology and structure of an individual nano-  
12 pillar from the etched FeCoB / NiFe stack. The HAADF STEM image (Fig. 1a) displays the  
13 general morphology of the nano-pillar with a distinct difference in Z-contrast between the top  
14 Ta mask and lower shaft. This is confirmed by EDX chemical mapping of Fig. 1b, revealing  
15 the dimensions of the NiFe section of the nano-pillar ( $\sim 60$  nm high, diameter of  $\leq 20$  nm), and  
16 that the  $\sim 3$  nm Ru layer separates it from the hard Ta mask. The O signal is dispersed across  
17 the entire nano-pillar and its physical state is explored through precession diffraction acquired  
18 from the boxed region (red) in the EDX chemical map of Fig. 1c. The precession data presented  
19 in Figs 1d & 1e is created by summing all the scanned diffraction patterns in the boxed region  
20 of Fig 1c into one diffraction pattern. Integrated signals are then extracted separately from the  
21 diffuse diffraction ring and crystalline diffraction spots to provide an overview of their  
22 respective contributions. The weakly crystalline / amorphous state of the surface of the nano-  
23 pillar highlighted in the scanned area of Fig. 1d (left) is demonstrated in the associated electron  
24 diffraction image (right). Conversely, Fig. 1e shows the crystalline state of the center of the  
25 nano-pillar in the scanned area (left) and associated electron diffraction (right). The line profile  
26 of Fig. 1f is acquired from the red arrow in Fig. 1c (averaged vertically over  $\sim 15$  nm) and  
27 displays the cross-section of normalized x-rays % for Fe, Ni and O content. The Ni and Fe  
28 profiles overlap consistently and the diffraction data of Fig. 1e demonstrates a homogeneous,  
29 crystalline NiFe core of the nano-pillar with measured composition of 81 at% Ni and 19 at%  
30 Fe. The O-rich phase is confined to the surface and considering its weakly crystalline /  
31 amorphous state, is largely attributed to residual organic resin from the preparation process.



1  
2 **Figure 1. Overview of the morphology, chemical composition and structural properties of the**  
3 **nano-pillar.** (a) HAADF STEM image of the nano-pillar; and (b) associated EDX chemical maps  
4 showing the elemental distribution of iron, nickel, ruthenium, tantalum and oxygen. (c) EDX chemical  
5 map highlighting the iron / nickel-rich center and oxygen-rich surface of the nano-pillar. (d,e) Precession  
6 electron diffraction acquired from the boxed region (red) in (c), showing the (d) amorphous surface; and  
7 (e) crystalline core. The colored scale bar denotes the normalized electron intensity between zero and  
8 maximum intensity. (f) Elemental line profile acquired along the red arrow in (c) and averaged vertically  
9 over  $\sim 15$  nm, displaying the cross-section of normalized x-rays % for iron, nickel and oxygen content.  
10

11 Figure 2 presents phase information reconstructed from electron holography of the nano-pillar,  
12 including quantification of magnetic induction and associated magnetization. The electron  
13 hologram of Fig. 2a shows the morphology of the nano-pillar at the same magnification as the  
14 associated projected magnetic induction map (Fig. 2b), which clearly demonstrates the  
15 existence of a magnetic dipole within the nano-pillar. This is emphasized by superimposing the  
16 associated magnetic induction over the EDX chemical map (Fig. 2c), where the magnetic  
17 contours flow along the major axis of the NiFe section. A line profile of the magnetic phase  
18 contribution ( $\phi_m$ ) acquired along the white arrow in Fig. 2c (averaged vertically over  $\sim 15$  nm)  
19 is overlaid over the chemical profile from the same region (Fig. 2d). The magnetic phase shift  
20  $\Delta\phi_m$  in the pillar can be used to quantify the integrated in-plane magnetic induction related to  
21 the nano-pillar, where the minimum and maximum  $\phi_m$  values [Fig. 2c, dotted vertical lines  
22 (pink)] coincide with the full width half maximum of the Ni / Fe chemical profiles. Extracting  
23 quantitative calculations of magnetization from such local observations must be handled with  
24 care as it displays integrated information (see Supplementary materials for details on the  
25 calculations summarized below). At first approximation, the nano-pillar can be treated as a

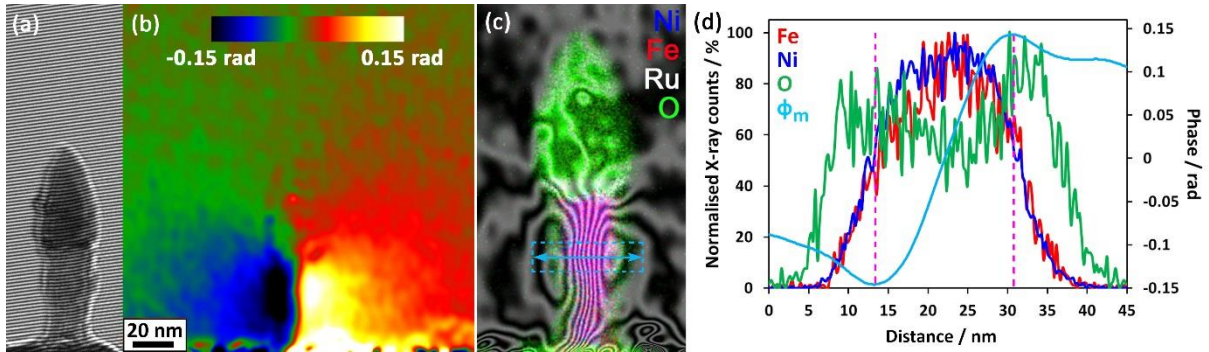
1 uniformly-magnetized infinite cylinder of radius  $r$ . The magnetic induction transverse to the  
2 electron beam direction is considered to arise from magnetization only (neglecting dipolar  
3 fields, *i.e.*, stray field and internal demagnetizing field) and can be estimated with the  
4 Aharonov-Bohm effect using a radius of  $\sim 8.6$  nm (obtained from Fig. 2d). A first value of  $\mu_0\mathbf{M}_s$   
5  $= 0.82 \pm 0.06$  T is extracted with the standard deviation determined from the noise of free space.  
6 To better quantify this important parameter, we can estimate the associated demagnetizing field  
7 of such a structure with the  $F_{ijk}$  functions from Hubert's formalism using a prism approach<sup>24</sup>, at  
8 the exact same location of the measurement of the integrated magnetic flux obtained with the  
9 phase slope. We then obtain a better estimation of  $\mu_0\mathbf{M}_s = 1.19 \pm 0.08$  T with the removal of  
10 the integrated demagnetizing and stray field globally antiparallel to magnetization, which  
11 lowered our first approximation. Subsequently, to overcome the geometrical approximation for  
12 the integrated demagnetizing field estimation with a prismatic geometry, we performed a  
13 tomographic reconstruction through inverse Abel transformation<sup>25</sup> to extract the magnetic flux  
14 density in the core vicinity of the cylinder. The resulting value was finally adjusted with the  
15 local estimation of demagnetizing field through  $F_{ijk}$  functions, as the tomography method helps  
16 to deconvolve the B field but not the internal  $H_d$ . Our final extraction leads to a value for the  
17 spontaneous magnetization induction of the NiFe nano-pillar of  **$\mu_0\mathbf{M}_s = 1.14 \pm 0.01$  T**.  
18 Considering the geometric approximation for the pillar is only estimated at one position of the  
19 structure, this value is substantially more precise and is in reasonable agreement with the  
20 spontaneous induction for a Ni<sub>81</sub>Fe<sub>19</sub> chemical composition, expected to reach 1.05 T<sup>26</sup>. We  
21 ascribe the difference to uncertainties related to the exact value of the composition of the alloy  
22 the diameter of the PSA, and the sharpness of its outer surface. Due the small size of the nano-  
23 pillar, the position along the nano-pillar axis of direct  $\phi_m$  measurement can also have a marked  
24 effect on the magnitude of the stray field, as shown in larger Co and Fe nanowires<sup>27</sup>. Being  
25 systematic, these errors are expected to have no impact on the thermomagnetic measurements  
26 reported in the following section. More details in our analysis of this quantification are given  
27 in the supplementary materials.

28

29

30

31

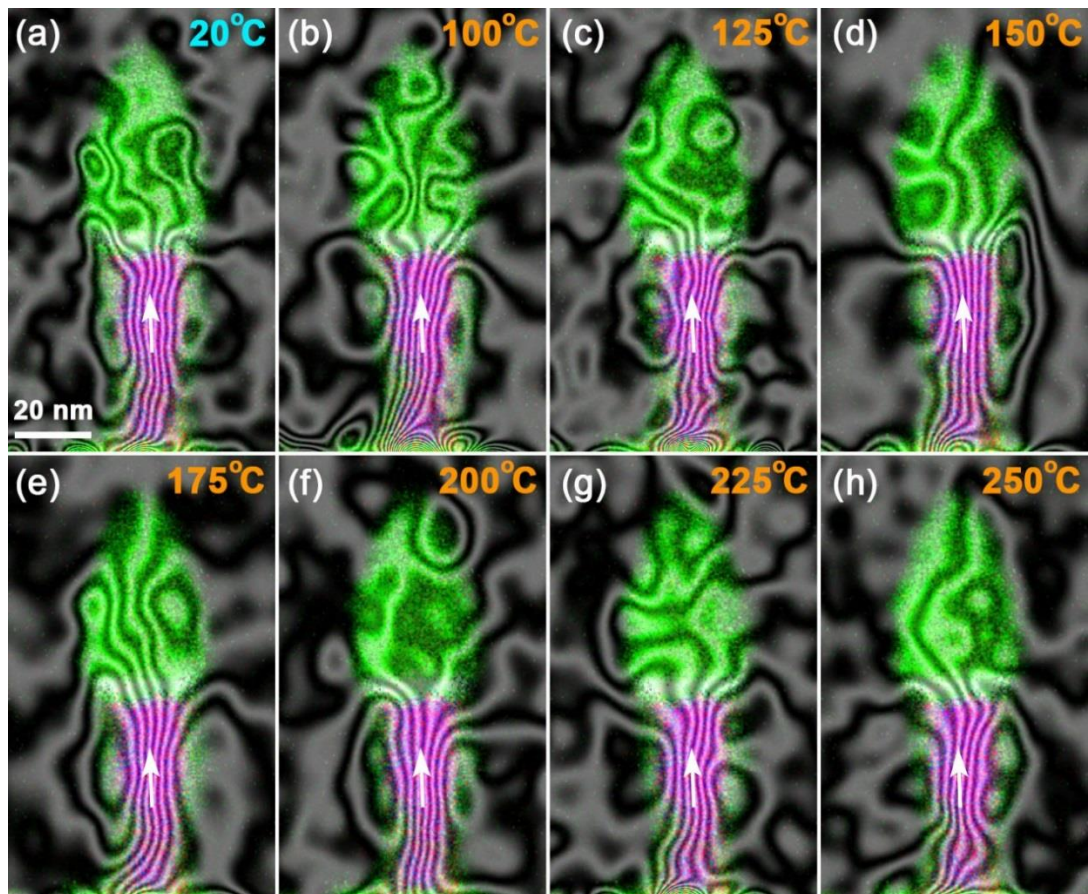


1  
 2 **Figure 2. Overview of the magnetic induction associated with the nano-pillar and its**  
 3 **quantification.** (a) Electron hologram of the nano-pillar; and (b) reconstructed magnetic contribution  
 4 to the total phase, revealing the PSA along its major axis. (c) Combined EDX / magnetic induction map  
 5 showing magnetic contours flowing along the major axis of the NiFe section. The contour spacing is  
 6 0.042 rad (cosine amplified by 150 times). (d) Line profile acquired along the white arrow in (c) and  
 7 averaged vertically over  $\sim 15$  nm around the mid-height of the PSA free layer, superimposing the cross-  
 8 section of magnetic phase over the chemical profile.

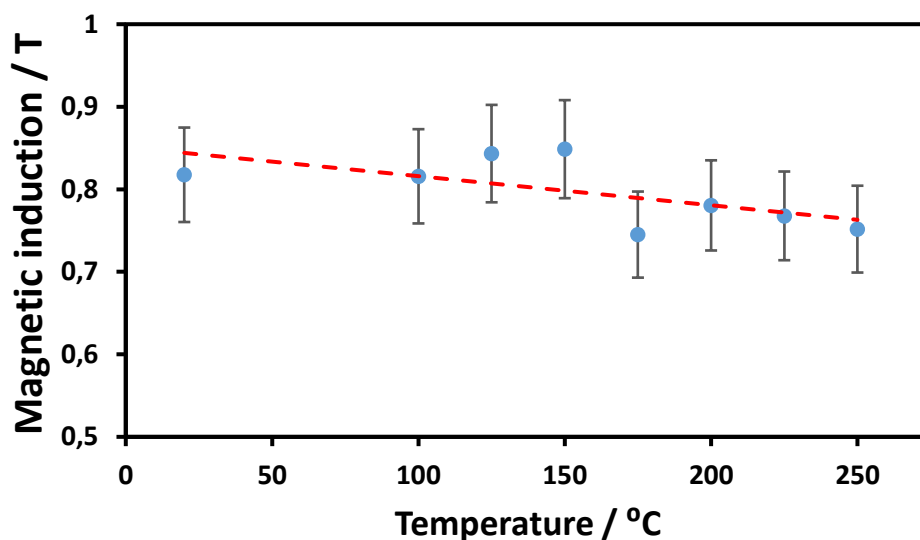
9

10 Figure 3 presents the thermomagnetic behavior of the nano-pillar during *in-situ* heating from  
 11 room temperature to 250 °C. The initial combined EDX / magnetic induction map of Fig. 3a  
 12 displays the nano-pillar at 20 °C, with the magnetization pointing from the bottom to the top of  
 13 the NiFe free layer and confirming its PSA. The associated magnetic induction maps of Figs  
 14 3b-h display the same nano-pillar during heating from 100 °C to 250 °C at 25 °C intervals. It is  
 15 evident that the NiFe section retains its upward direction of magnetization at all temperatures  
 16 up to 250 °C. The thermomagnetic stability of the NiFe section in the nano-pillar is supported  
 17 by Figure 4, which presents corresponding quantitative measurements of magnetic induction at  
 18 each temperature interval. The  $\Delta\phi_m$  was measured from the same area presented in Fig. 2c,d  
 19 and  $\vec{B}$  calculated using equation S2 (Supplementary information), which is proportional to  
 20 magnetization. The average value of  $B^{\rightarrow}$  is  $\sim 0.8 \pm 0.06$ T and the trend-line exhibits a decrease  
 21 of  $\sim 0.08$ T between 20 °C and 250 °C, which is in good agreement with a  $\sim 0.09$ T decrease over  
 22 the same temperature range in bulk permalloy ( $\text{Ni}_{80}\text{Fe}_{20}$ )<sup>28,29</sup>. If heated to higher temperatures,  
 23 the nano-pillar would be expected to follow the same bulk properties and become paramagnetic  
 24 at a Curie temperature around  $\sim 575$  °C<sup>28,29</sup>. As the contribution of the dipolar field to the  
 25 measured induction field is proportional to magnetization for PSA, we expected that Fig.4 is  
 26 representative of the thermal decay of magnetization in the PSA.

27



1  
 2 **Figure 3. Visualization of the thermomagnetic stability within the nano-pillar.** (a-h) Combined  
 3 EDX / magnetic induction maps showing the PSA in the NiFe section of the nano-pillar acquired at (a)  
 4 20 °C; or during *in-situ* heating at 25 °C intervals from (b) 100 °C to (h) 250 °C. The contour spacing is  
 5 0.042 rad for all the magnetic induction maps (cosine multiplied by 150 times) and the magnetization  
 6 direction is shown using arrows.  
 7



8  
 9 **Figure 4. Magnetic induction associated to the nano-pillar as a function of temperature.** Calculated  
 10 magnetic induction transverse to the electron beam using the direct measurement of magnetic  
 11 contribution to the phase from the NiFe section shown in Figure 3 with temperature, i.e., including a  
 12 contribution from the demagnetizing and stray fields globally opposite to magnetization in the pillar,  
 13 from 20 °C to 250 °C.

#### 1 **4. Discussion**

2 The main reason to fabricate STT-MRAM nano-pillars with PSA is to stabilize and preserve  
3 the magnetic configuration of the free FeCoB / NiFe composite layer in response to temperature  
4 fluctuations during operation. It is evident from the *in-situ* heating TEM experiment that the  
5 dipolar magnetic orientation along the major axis of the NiFe section (bottom to top) is retained  
6 at all temperature intervals up to at least 250 °C. In addition, the associated direct measurements  
7 of  $\vec{B}$  (average  $\approx 0.8\text{T} \pm 0.06\text{T}$ ) did not vary sufficiently to suggest a change in magnetic  
8 orientation, nor magnetization. The slight decreasing trend in magnitude of  $\vec{B}$  is attributed to an  
9 expected reduction in spontaneous magnetization when heating towards the Curie  
10 temperature<sup>30</sup>, as would be observed in the same bulk material. As the shape-anisotropy energy  
11 barrier of the nano-pillar scales linearly with  $M_s^2$ , this confirms that the energy barrier of  
12 switching between parallel and anti-parallel states has not been exceeded up to at least 250 °C,  
13 and the PSA has provided significant thermal stability compared to standard p-STT-MRAM  
14 stacks based on ultrathin films<sup>12-15</sup>. In standard p-STT-MRAM, the spontaneous magnetization  
15 may indeed decrease by a few tens of percent at 250°C due to enhanced fluctuations in low-  
16 dimensions for the ultrathin films involved, and the energy barrier associated with  
17 perpendicular anisotropy may decrease even more as it relies on interfacial magnetic  
18 anisotropy, which suffers from enhanced thermal decay due to its two-dimensional nature<sup>31-33</sup>.  
19 Further, the maximum temperature of *in-situ* heating used (250 °C) far exceeds the operating  
20 temperatures for a range of STT-MRAM device applications, including commercial (70 °C),  
21 industrial (85 °C), automotive (125 °C) and military (150 °C)<sup>34</sup>. It is also comparable to the  
22 temperature of reflow soldering used to attach chips to a printed circuit board (260 °C)<sup>35</sup>. This  
23 thermal stability is crucial for many FLASH-replacement applications in which the program  
24 code is loaded in the chip prior to reflow soldering.

25 In conclusion, this electron holography study has provided explicit evidence of the PSA in  
26  $\leq 20$  nm diameter p-STT-MRAM nano-pillar; previously only measured indirectly by  
27 magnetoresistance measurements and micromagnetic modelling. The enhanced thermal  
28 stability of PSA-STT-MRAM, compared with standard p-STT MRAM based on these films,  
29 has been confirmed by both imaging and quantitative measurements from their magnetic  
30 configuration during *in-situ* heating. This supports the use of PSA-STT-MRAM in a variety of  
31 applications that require reliable performance over a range of operating temperatures.

32

33

## 1 **5. Supporting Information**

2 Dipolar field calculation (S1) and quantitative phase analysis (S2).

3

## 4 **6. References**

- 5 1. B. Dieny, *et al.*, Opportunities and challenges for spintronics in microelectronics  
6 industry, *Nat. Electron.* 2020, **3**, 446-459.
- 7 2. S. Bhatti, *et al.*, Spintronics based random access memory: a review, *Mater. Today.*  
8 2017, **20**, 530-548.
- 9 3. S. Ikeda, *et al.*, A perpendicular-anisotropy CoFeB–MgO magnetic tunnel junction, *Nat.*  
10 *Mater.*, 2010, **9**, 721.
- 11 4. A. D. Kent, Spintronics: Perpendicular all the way, *Nat. Mater.*, 2010, **9**, 699.
- 12 5. T. Liu, Y. Zhang, J. W. Cai and H. Y. Pan, Thermally robust Mo/CoFeB/MgO trilayers  
13 with strong perpendicular magnetic anisotropy, *Sci. Rep.*, 2015, **4**, 5895.
- 14 6. D. McGrath, Intel says FinFET-based embedded MRAM is production-ready. EE Times  
15 (20 February 2019); <https://go.nature.com/3gQyWzf>.
- 16 7. Apalkov, D., Dieny, B. & Slaughter, J. M. Magnetoresistive random access memory.  
17 *Proc. IEEE*, 2016, **104**, 1796–1830.
- 18 8. Khvalkovskiy, A. V. et al. Basic principles of STT-MRAM cell operation in memory  
19 arrays. *J. Phys. D.* 2013, **46**, 074001.
- 20 9. S.-W. Chung, T. Kishi, J.W. Park, M. Yoshikawa, K. S. Park, T. Nagase, K. Sunouchi,  
21 H. Kanaya, G.C. Kim, K. Noma, M. S. Lee, A. Yamamoto, K. M. Rho, K. Tsuchida, S.  
22 J. Chung, J. Y. Yi, H. S. Kim, Y.S. Chun, H. Oyamatsu and S. J. Hong, *Proceedings of*  
23 *the 2016 IEDM conference*, 2016, 27.1.
- 24 10. B. Dieny and M. Chshiev, Perpendicular magnetic anisotropy at transition metal/oxide  
25 interfaces and applications. *Rev. Mod. Phys.*, 2017, **89**, 025008.
- 26 11. V. D. Nguyen, P. Sabon, J. Chatterjee, L. Tille, P. Veloso Coelho, S. Auffret, R. Sousa,  
27 L. Prejbeanu, E. Gautier, L. Vila and B. Dieny, Novel approach for nano-patterning  
28 magnetic tunnel junctions stacks at narrow pitch: A route towards high density STT-  
29 MRAM applications, *2017 IEEE International Electron Devices Meeting (IEDM)*,  
30 2017, DOI: 10.1109/IEDM.2017.8268517.
- 31 12. N. Perrissin, S. Lequeux, N. Strelkov, A. Chavent, L. Vila, L. D. Buda-Prejbeanu, S.  
32 Auffret, R. C. Sousa, I. L. Prejbeanu and B. Dieny, A highly thermally stable sub-20  
33 nm magnetic random-access memory based on perpendicular shape anisotropy,  
34 *Nanoscale*, 2018, **10**, 12187.

- 1 13. K. Watanabe, B. Jinnai, S. Fukami, H. Sato and H. Ohno, Shape anisotropy revisited in  
2 single-digit nanometer magnetic tunnel junctions, *Nat. Commun.* 2018, **9**, 663.
- 3 14. N. Perrissin, N. Caçoilo, G. Gregoire, S. Lequeux, L. Tillie, N. Strelkov, A. Chavent, S.  
4 Auffret, L. D. Buda-Prejbeanu, R. C. Sousa, L. Vila, I. L. Prejbeanu and B. Dieny,  
5 Perpendicular shape anisotropy spin transfer torque magnetic random-access memory:  
6 towards sub-10 nm devices. *J. Phys. D: Appl. Phys.*, 2019, **52**, 505005.
- 7 15. S. Lequeux, N. Perrissin, G. Grégoire, L. Tillie, A. Chavent, N. Strelkov, L. Vila, L. D.  
8 Buda-Prejbeanu, S. Auffret, R. C. Sousa, I. L. Prejbeanu, E. Di Russo, E. Gautier, A. P.  
9 Conlan, D. Cooper and B. Dieny, Thermal robustness of magnetic tunnel junctions with  
10 perpendicular shape anisotropy, *Nanoscale*, 2020, **12**, 6378.
- 11 16. V. Boureau, M. Stano, J-L. Rouvière, J-C. Toussaint, O. Fruchart and D. Cooper, High-  
12 sensitivity mapping of magnetic induction fields with nanometer-scale resolution:  
13 comparison of off-axis electron holography and PDPC, *J. Phys. D: Appl. Phys.* 2021,  
14 **54**, 085001.
- 15 17. T. P. Almeida, T. Kasama, A. R. Muxworthy, W. Williams, and R. E. Dunin-Borkowski,  
16 Observing thermomagnetic stability of non-ideal magnetite particles: Good  
17 paleomagnetic recorders? *Geophys. Res. Lett.* 2014, **41**, 7041.
- 18 18. T. P. Almeida, A. R. Muxworthy, A. Kovács, W. Williams, P. D. Brown, and R. E.  
19 Dunin-Borkowski, Direct visualization of the thermomagnetic behavior of pseudo-  
20 single-domain magnetite particles, *Sci. Adv.* 2016, **2**, e1501801.
- 21 19. T. P. Almeida, A. R. Muxworthy, A. Kovács, W. Williams, L. Nagy, P. Ó Conbhuí, C.  
22 Frandsen, R. Supakulopas, and R. E. Dunin-Borkowski, Direct observation of the  
23 thermal demagnetization of a vortex structure held by a non-ideal magnetite recorder,  
24 *Geophys. Res. Lett.* 2016, **43**, 8426.
- 25 20. J. Shah, W. Williams, T. P. Almeida, L. Nagy, A. R. Muxworthy, A. Kovács, M. A.  
26 Valdez-Grijalva, K. Fabian, S. S. Russell, M. J. Genge and R. E. Dunin-Borkowski,  
27 The oldest magnetic record in our solar system identified using nanometric imaging and  
28 numerical modeling, *Nat. Commun.* 2018, **9**, 1173.
- 29 21. V. Boureau, V. D. Nguyen, A. Masseboeuf, A. Palomino, E. Gautier, J. Chatterjee, S.  
30 Lequeux, S. Auffret, L. Vila, R. Sousa, L. Prejbeanu, D. Cooper and B. Dieny, An  
31 electron holography study of perpendicular magnetic tunnel junctions nanostructured  
32 by deposition on pre-patterned conducting pillars, *Nanoscale*, 2020, **12**, 17312.

- 1 22. V. Boureau, R. McLeod, B. Mayall and D. Cooper, Off-axis electron holography  
2 combining summation of hologram series with double-exposure phase-shifting: Theory  
3 and application, *Ultramicroscopy*, 2018, **193**, 52-63.
- 4 23. T. P. Almeida, T. Kasama, A. R. Muxworthy, W. Williams, L. Nagy, T. W. Hansen, P.  
5 D. Brown and R. E. Dunin-Borkowski, Visualized effect of oxidation on magnetic  
6 recording fidelity in pseudo-single-domain magnetite particles, *Nat. Commun.* 2014, **5**,  
7 5154.
- 8 24. A. Hubert and R. Schafer, *Magnetic Domains. The Analysis of Magnetic*  
9 *Microstructures*, Springer-Verlag, Berlin, Heidelberg, New York, 1998.
- 10 25. C. Phatak, L. de Knoop, F. Houdellier, C. Gatel, M. J. Hÿtch and A. Masseurboeuf,  
11 Quantitative 3D electromagnetic field determination of 1D nanostructures from single  
12 projection, *Ultramicroscopy*, 2016, **164**, 24-30.
- 13 26. R. D. Tikhonov and A. A. Cheremisinov, Magnetization of Permalloy Films, *Russian*  
14 *Microelectronics*, 2017, **46 (2)**, 95–104.
- 15 27. K. Chai, Z. Li, W. Huang, G. Richter, R. Liu, B. Zou, J. Caron, A. Kovács, R. E. Dunin-  
16 Borkowski and J. Li, Magnetic quantification of single-crystalline Fe and Co nanowires  
17 via off-axis electron holography, *J. Chem. Phys.* 2020, 152, 114202.
- 18 28. A. B. Johnston, J. N. Chapman, B. Khamsehpour and C. D. W. Wilkinson, *In situ* studies  
19 of the properties of micrometre-sized magnetic elements by coherent Foucault imaging,  
20 *J. Phys. D: Appl. Phys.* 1996, **29**, 1419–1427.
- 21 29. R. M. Bozorth, 1964 *Ferromagnetism* (New York: Van Nostrand) p 112.
- 22 30. X. Zhang, Y. Lao, J. Sklenar, N. S. Bingham, J. T. Batley, J. D. Watts, C. Nisoli, C.  
23 Leighton and P. Schiffer, Understanding thermal annealing of artificial spin ice, *APL*  
24 *Mater.* 2019, **7**, 111112.
- 25 31. H. Sato, E. C. I. Enobio, M. Yamanouchi, S. Ikeda, S. Fukami, S. Kanai, F. Matsukura  
26 and H. Ohno, Properties of magnetic tunnel junctions with a  
27 MgO/CoFeB/Ta/CoFeB/MgO recording structure down to junction diameter of 11 nm  
28 *Appl. Phys. Lett.*, 2014, **105**, 062403.
- 29 32. H. Sato, S. Ikeda and H. Ohno, Magnetic tunnel junctions with perpendicular easy axis  
30 at junction diameter of less than 20 nm *Jpn. J. Appl. Phys.*, **2017**, 56, 0802A6.
- 31 33. L. Thomas, G. Jan, J. Zhu, H. Liu, Y.-J. Lee, S. Le, R.-Y. Tong, K. Pi, Y.-J. Wang, D.  
32 Shen, R. He, J. Haq, J. Teng, V. Lam, K. Huang, T. Zhong, T. Torng and P.-K. Wang,  
33 Perpendicular spin transfer torque magnetic random access memories with high spin

1 torque efficiency and thermal stability for embedded applications (invited), *J. Appl.*  
2 *Phys.*, 2014, **115**, 172615.

3 34. J. M. Iwata-Harms, G. Jan, H. Liu, S. Serrano-Guisan, J. Zhu, L. Thomas, R-Y. Tong,  
4 V. Sundar and P-K. Wang, High-temperature thermal stability driven by magnetization  
5 dilution in CoFeB free layers for spin-transfer torque magnetic random access memory,  
6 *Sci. Rep.* 2018, **8**, 14409.

7 35. Meng-Chun Shih et al., "Reliability study of perpendicular STT-MRAM as emerging  
8 embedded memory qualified for reflow soldering at 260°C," *2016 IEEE Symposium on*  
9 *VLSI Technology*, 2016, pp. 1-2, doi: 10.1109/VLSIT.2016.7573411.

## 10 **Funding**

11 CEA-Leti is a Carnot Institute. This work was supported by the French ANR via Carnot funding  
12 and the European Research Council (ERC MAGICAL, 669204).

13